Adaptive PID Control for Hydraulic Turbine Regulation Systems Based on INGWO and BPNN

Jinbao Chen, Gang He, Yunhe Wang, Yang Zheng, and Zhihuai Xiao

Abstract—To ensure system stability, the fixed-PID (F-PID) controller with small parameters is usually adopted in hydropower stations. This involves a slow setting speed and it is difficult to realize optimal control for full working conditions. To address the problem, this paper designs a variable-PID (V-PID) controller for a hydraulic turbine regulation system (HTRS) based on the improved grey wolf optimizer (INGWO) and back propagation neural networks (BPNN). These can achieve excellent regulation under full working conditions. First, the nonlinear HTRS model containing the nonlinear hydro-turbine model is constructed and the stable domain is obtained using Hopf bifurcation theory to determine the available range of PID parameters. The optimal PID parameters in typical working conditions are then calculated by the INGWO, and the optimal PID parameters are generalized through training the V-PID neural networks which take the optimal PID parameters as sample data. The V-PID neural networks with different structures are compared to determine the optimal structure of the variable-PID controller model. The V-PID controller-based nonlinear HTRS model shows that the PID parameters can be automatically adjusted online according to the working condition changes, realizing optimal control of hydropower units in full working conditions.

Index Terms—Hydraulic turbine regulation system, back propagation neural networks, Hopf bifurcation, grey wolf optimizer, variable-PID controller.

I. INTRODUCTION

In the modern power system, hydropower units mainly undertake tasks such as black start, cold and hot standby, peak shaving, and frequency modulation, so their stability and regulation play important roles in promoting the consumption of new energy [1], [2], as schematically shown in Fig. 1. However, the access of large-scale intermittent energy to the grid leads to frequent switching of operating conditions of hydropower units, resulting in higher requirements for their stability and regulation performance.

A proportional-integral-differential (PID) controller with a simplified structure is often used in the hydraulic turbine regulation system (HTRS) to ensure the stability of the hydropower units [3]–[5]. However, the HTRS contains the complex nonlinearity, and the requirements of system performance on PID parameters make it difficult to be consistent in different operating conditions [6], [7]. To ensure stability, the governors of most hydropower stations often set one or several groups of smaller PID parameters in advance according to different control modes, and keep the control parameters unchanged during operation [8], [9]. Thus, the HTRS does not have good regulation in most working conditions. Considering the requirements of system regulation performance in full operating conditions, the fixed-PID (F-PID) control obviously cannot meet the needs.

To solve this problem, much work has been done on the optimization of the PID controller. This can be categorized into F-PID optimization and variable-PID (V-PID) design. For the F-PID optimization, various algorithms have been adopted. Reference [10] uses the particle swarm optimization (PSO) to obtain optimal parameters to achieve good control of the decentralized digital model in the load frequency control model (LFC). The simulation results reveal that the optimized controller satisfies the stability requirements of LFC and has superior dynamic response. Reference [11] applies the improved gravitational search algorithm to optimize the controller parameters of a pumped storage power station to make the regulation system faster in the unbalanced area, whereas [12] adopts an improved genetic algorithm to search optimal controller parameters in no-load and load turbulence conditions. In [13], the modified gravitational search algorithm is applied to optimize the fractional-order PID parameters for better-regulating quality in low water head conditions. Clearly, F-PID optimization still cannot achieve the required regulation performance under full

Jinbao Chen is with the China Yangtze River Electric Power Co., Ltd., Wuhan 430000, China and the School of Power and Mechanical Engineering, Wuhan University, Wuhan 430072, China (13253681095@163.com).

Gang He is with the Hebei Fengning Pumped Storage Co., Ltd., Chengde 050300, China (ganghe2022@163.com).

Yunhe Wang, Yang Zheng, and Zhihuai Xiao (corresponding author) are with the School of Power and Mechanical Engineering, Wuhan University, Wuhan 430072, China (2889973626@qq.com; zhengyang@whu.edu.cn; xiaozhihuai@126.com).

working conditions. Moreover, these algorithms contain many artificially given parameters according to experience. If the values of these parameters are too large, the calculation time will undoubtedly increase. On the other hand, the optimal solution will be easily missed if these parameters are too small.
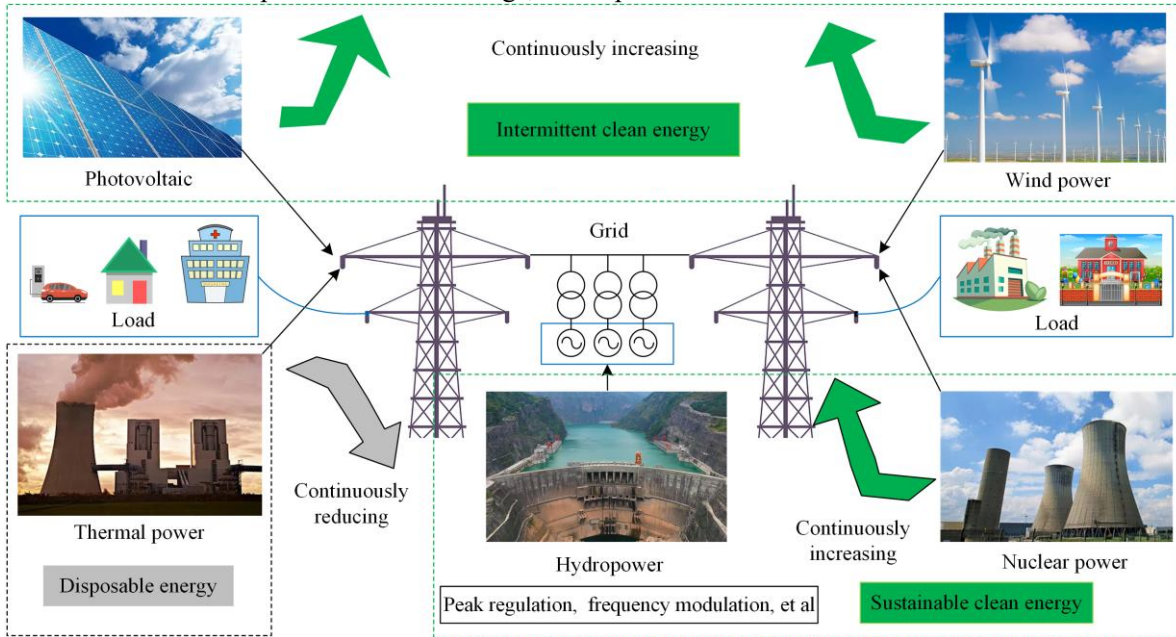

Fig. 1. Role of hydropower in the modern power system.

For V-PID controller design, predictive control is widely used. This generally takes the deviation between the current value of the given signal, the feedback signal, and the historical value of the feedback signal as the input, to calculate the system output with complex control algorithms. Reference [14] designs the predictive-fuzzy PID controller to avoid deep running into the 'S' characteristic area of the pumped storage unit, while [15] proposes a PID predictive controller with delays based on the state space model. In [16], an online trained neural network-based PID predictive controller is designed to achieve global optimal control of HTRS, whereas [17] proposes a predicted fuzzy PID controller to obtain a stable control effect in low water head conditions. However, although these control modes can give proper PID parameters for HTRS in different working conditions, the control effect is usually poor during online training, i.e., the optimal controller parameters cannot be obtained in real-time. This problem is also reflected in advanced control algorithms such as generalized predictive control. Therefore, in practice, predictive control is difficult to apply to HTRS. Therefore, it is necessary to design an intelligent controller without requiring online training, one has a simplified structure and the ability to adaptively adjust control parameters.

Hopf bifurcation [6] is an important theory in the study of the stability of nonlinear systems. It can give the relationship that the controller parameters should meet for the system to remain stable, i.e., the constraint conditions. Thus, based on these constraint conditions, it can be judged whether PID parameters can ensure the sta-

bility of the system. Consequently, if the controller constraints are considered when optimizing the PID parameters, the variation range of the PID parameters can be limited directly, and unnecessary calculation outside the range of the system stability domain can be avoided. The grey wolf optimizer (GWO), developed in recent years, shows excellent performance in dealing with nonlinear problems compared with conventional algorithms [18]. Therefore, an improved GWO algorithm based on Hopf bifurcation theory is proposed in this paper to optimize the PID parameters in typical working conditions, and to improve calculation efficiency and accuracy. Also, a V-PID controller for HTRS based on back propagation neural networks (BPNN) [6], [19] is proposed. This takes the optimal PID parameters as sample data to achieve excellent regulation in full working conditions while ensuring stability. The V-PID controller-based nonlinear HTRS model shows that the PID parameters can be automatically adjusted online according to the changes of the working conditions, realizing the optimal control of hydropower units.

In summary, the main contributions of this study include:

1) The advantage of GWO with the nonlinear iterative coefficient is proved through comparative tests based on test functions.

2) An improved GWO based on Hopf bifurcation theory is proposed to obtain the training data of the V-PID controller neural network.

3) The V-PID controller model with optimal structure is determined through theoretical analysis and quantitative calculation.

The rest of this paper is organized as follows. Section II introduces the modeling method of nonlinear HTRS. In Section III, the design method of the V-PID controller is introduced in detail, while Section IV illustrates the advantages of the V-PID controller through simulation verification. The conclusion is drawn in Section V.

II. MODELING OF NONLINEAR HTRS

The nonlinear HTRS model includes the diversion system, hydro-turbine, controller, and generator [20], [21].

A. Diversion System Model

The diversion system model depends on the length of the diversion pipeline. In this paper, the length of the diversion pipeline is less than 600 m, so the rigid water hammer model is enough to meet the accuracy requirements [22], expressed as:

$$G_h(s) = -T_w s \qquad (1)$$

where T_w is the water inertia time constant.

B. Hydro-turbine Model

The BPNN has strong data fitting ability and can be used to build nonlinear models. This is described in detail in [23]. In the process of modeling, the mean square error (M_{SE}) given by (2) is usually chosen as the fitness function, and the weight and threshold of the BPNN are continuously adjusted by the gradient descent method to make the model output approximate the expected output [23].

$$M_{SE} = \frac{\sum_{i=1}^{k}(\hat{D}_i - D_i)^2}{k} \qquad (2)$$

where k represents the number of sample data; $\hat{D}_i$ represents the prediction data; and D_i represents the sample data.

To prevent the network from blindly pursuing precision requirements and over-fitting, the maximal generation is set to 1000, and the validation check time is set to 6, i.e., the network reaches the termination condition and stops learning in time if the network passes 6 consecutive validation checks or the generation reaches 1000.

To reduce the modeling time of the V-PID controller and take into account modeling accuracy, the piecewise linearization hydro-turbine model based on the BPNN [24] is adopted to calculate the stable domain of the HTRS, and the nonlinear hydro-turbine model based on the BPNN is adopted to obtain the optimal parameters of the PID controller. In addition, it should be noted that the verification and test data are the same as the training data because the actual operation data will be used for verifying the hydro-turbine model after modeling.

1) Nonlinear Hydro-turbine Model Based on BPNN

To accurately describe the real characteristics of the hydro-turbine, the nonlinear hydro-turbine model is established based on the BPNN with the prototype turbine test data. Figure 2 gives the modeling process [3] which can be divided into the following steps: 1) obtain and supplement the test data of the prototype hydro-turbine, and obtain the training samples of discharge and torque characteristics neural networks (DCNN and TCNN); 2) combine the actual operational data with the GWO to correct the guide vane opening Y of hydro-turbine test data; and 3) construct the nonlinear hydro-turbine model containing the DCNN and TCNN based on the BPNN. In Fig. 2, $\gamma = \rho g$, where ρ is the density of water and g is the acceleration due to gravity. '$Y = Y(n_{11}, M_{11})$' and '$\eta = \eta(n_{11}, M_{11})$' are the Y and η characteristics neural networks respectively; n_{11} is the unit speed which satisfies (3); Q_{11} is the unit discharge; and M_{11} is the unit torque.

$$n_{11} = \frac{XD}{\sqrt{H}} \qquad (3)$$

where D is the diameter of the runner; H is the working head; and X is the rotational speed.

2) Piecewise Linear Hydro-turbine Model Based on BPNN

As the dynamic characteristics of the hydro-turbine can be approximately expressed by Q and M_t when it is in the steady state [6], a piecewise linear hydro-turbine model can be constructed by converting the outputs of the DCNN and TCNN into the discharge Q and torque M_t through (4) and (5), and then calculating the transfer coefficients of the hydro-turbine in different working conditions.

$$Q = Q_{11} D^2 \sqrt{H} \qquad (4)$$

$$M_t = M_{11} D^3 H \qquad (5)$$

For the Francis turbine, the dynamic characteristics are all nonlinear functions of Y, X, and H [25], expressed as:

$$\begin{cases} Q = Q(Y, X, H) \\ M_t = M_t(Y, X, H) \end{cases} \qquad (6)$$

In the small fluctuation operational condition, the Taylor expansion is carried out for hydro-turbine discharge and torque characteristics at the working point, and the higher-order trace above the second order is ignored to obtain the algebraic equation of constant coefficients of the piecewise linear hydro-turbine model [6], as:

$$\begin{cases} q = e_{qy} y + e_{qx} x + e_{qh} h \\ m_t = e_y y + e_x x + e_h h \end{cases} \qquad (7)$$

where q, y, x, h, and m_t are the deviation relative values of Q, Y, X, H, and M_t, respectively; e_{qy}, e_{qx}, and e_{qh} are the transfer coefficients of q to y, x, and h, respectively; e_y, e_x, and e_h are the transfer coefficients of m_t to y, x, and h, respectively.
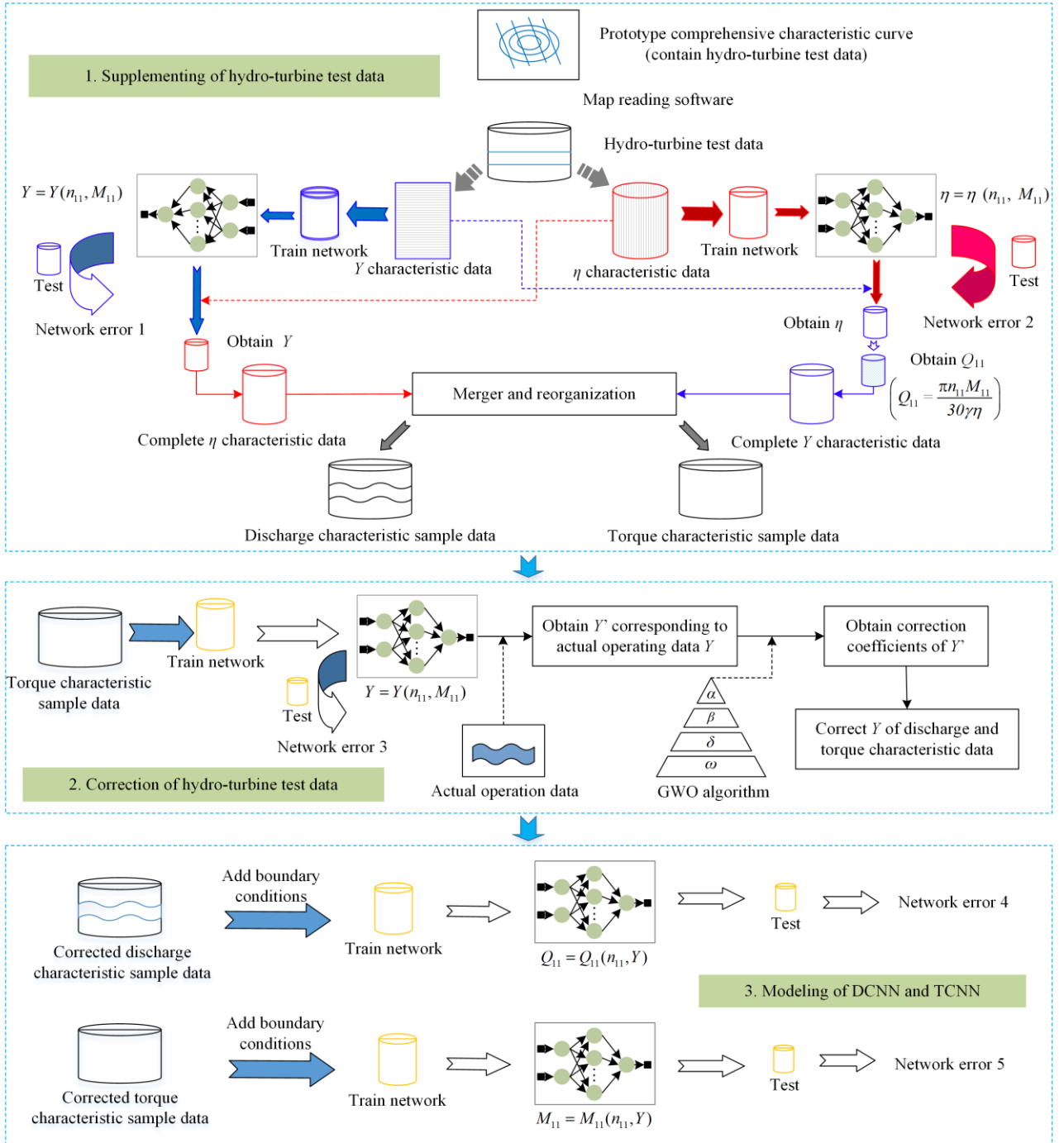
Fig. 2. Modeling process of nonlinear hydro-turbine model.

The transfer coefficients of the hydro-turbine can be calculated as:

$$
\begin{aligned}
e_{qy} = \frac{\partial \dfrac{Q}{Q_r}}{\partial \dfrac{Y}{Y_{\max}}}, \quad
e_{qx} = \frac{\partial \dfrac{Q}{Q_r}}{\partial \dfrac{X}{X_r}}, \quad
e_{qh} = \frac{\partial \dfrac{Q}{Q_r}}{\partial \dfrac{H}{H_r}}, \\[2ex]
e_y = \frac{\partial \dfrac{M_t}{M_r}}{\partial \dfrac{Y}{Y_{\max}}}, \quad
e_x = \frac{\partial \dfrac{M_t}{M_r}}{\partial \dfrac{X}{X_r}}, \quad
e_h = \frac{\partial \dfrac{M_t}{M_r}}{\partial \dfrac{H}{H_r}}
\end{aligned}
\tag{8}
$$

where M_r is the rated M_t; X_r is the rated X; Q_r is the rated Q; H_r is the rated H; and $Y_{\max}$ is the maximum Y.

It should be noted that the change of X is not considered in power control mode (PCM), i.e., equation (7) can be expressed as:

$$
\begin{cases}
q = e_{qy}y + e_{qh}h \\
m_t = e_y y + e_h h
\end{cases}
\tag{9}
$$

C. Governor Model

The governor of the hydropower station includes the controller and electro-hydraulic servo system [26]–[28].

Therein, there are series and parallel controllers. This paper studies the parallel PID type under PCM, as shown in Fig. 3, where e_p is the adjustment rate; p_c is the reference value of the power; p_t is the feedback of power; f_c is the reference value of the frequency; and f_e is the feedback frequency; u is the output of the controller; e is the tracking error of the system variable, while K_P, K_I, and K_D are links of proportional, integral and differential gains, respectively; T_{1v} is the time constant of the differential link, which is not considered in this paper; and T_y is the reaction time constant of the main servomotor.
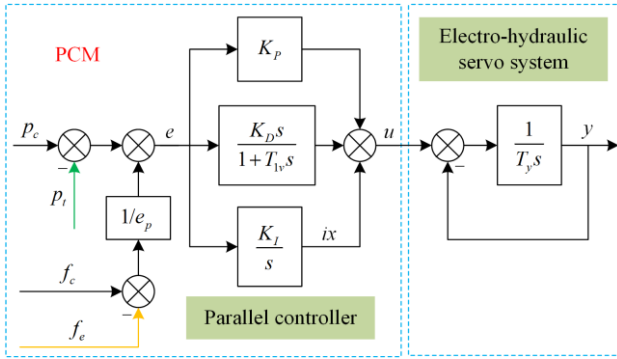
Fig. 3. Parallel PID controller.

The transfer functions of the controller $G_c(s)$ and the electro-hydraulic servo system $G_e(s)$ are given as:

$$G_c(s) = \frac{u}{e} = \frac{(K_D + T_{1v}K_P)s^2 + (K_P + T_{1v}K_I)s + K_I}{T_{1v}s^2 + s} \quad (10)$$

$$G_e(s) = \frac{y}{u} = \frac{1}{T_y s + 1} \quad (11)$$

D. Generator Model

The classical second-order generator model [29] is adopted, expressed as:

$$\begin{cases} \dot{\varphi} = \omega_0 \omega_G \\ \dot{\omega}_G = (m_t - m_e - K\omega_G)/T_a \end{cases} \quad (12)$$

where φ is the angle of the generator rotor; ω_0 is the synchronous angular velocity; ω_G is the relative deviation of the generator speed; K is the damping coefficient of the generator; and T_a is the inertia time constant of the unit.

If the damping coefficient of the generator includes the influence of the unit speed change on the torque, the electromagnetic torque m_e can be used to represent electromagnetic power P_e [30], i.e.,

$$m_e = P_e \quad (13)$$

$$P_e = \frac{E_q V_s}{X_{ds}} \sin \dot{\varphi} + \frac{V_s^2}{2} \frac{(X_{ds} - X_{qs})}{X_{ds} X_{qs}} \sin 2\dot{\varphi} \quad (14)$$

where E_q is the q-axis transient potential; V_s is the infinite bus voltage; while X_{ds} and X_{qs} are the d-axis and q-axis transient reactance, respectively.

E. Nonlinear HTRS Model

Figure 4 shows the nonlinear HTRS model under PCM, where $f_c = 0$, $p_c = 0$, $K_D = 0$; M_0 is the initial M_t; and Q_0 is the initial Q.
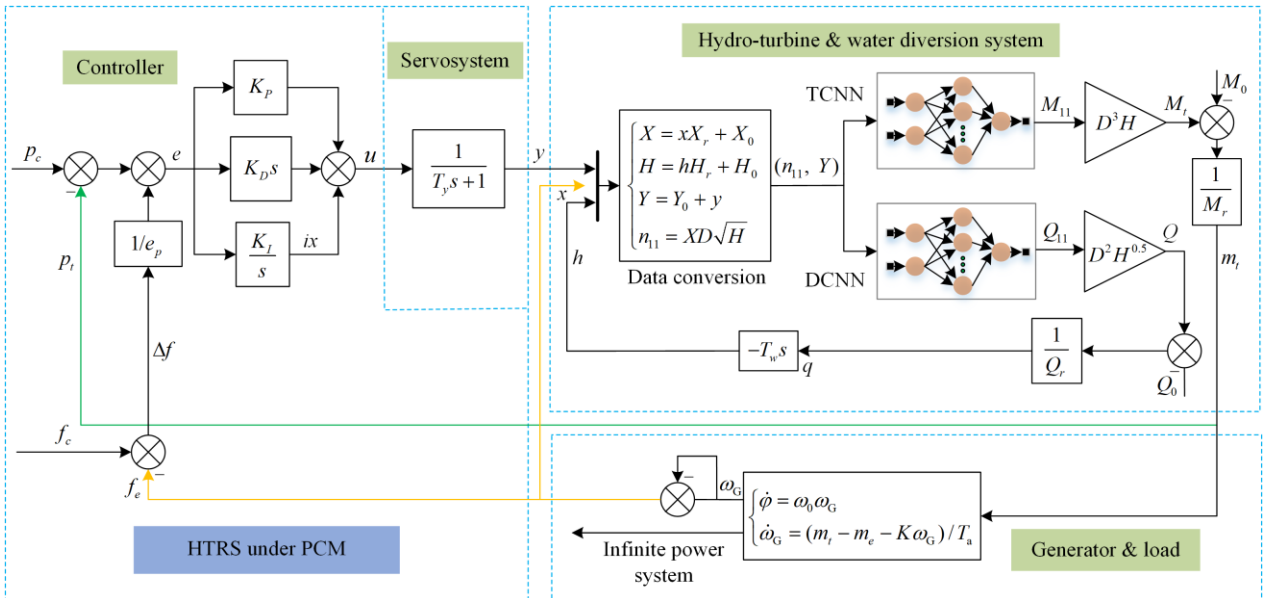

Fig. 4. Nonlinear HTRS model based on BPNN under PCM.

III. V-PID Controller Based on BPNN

The neural network-based V-PID controller includes K_P, K_I, and K_D neural networks, and include the input, hidden, and output layers. The input layer is composed of H and Y, and the output layer is K_P, K_I, or K_D. The design process of the V-PID controller is shown in Fig. 5, where H_{min} and H_{max} are the minimum and maximum H, respectively; $Y_{no\text{-}load}$ is the Y in no-load conditions, while H_D and Y_D are the intervals used to divide H and Y, respectively; f_1, f_2, and f_3 are the functions constructed based on the BP neural network with Y and H as the input and K_P, K_I, or K_D as the output.
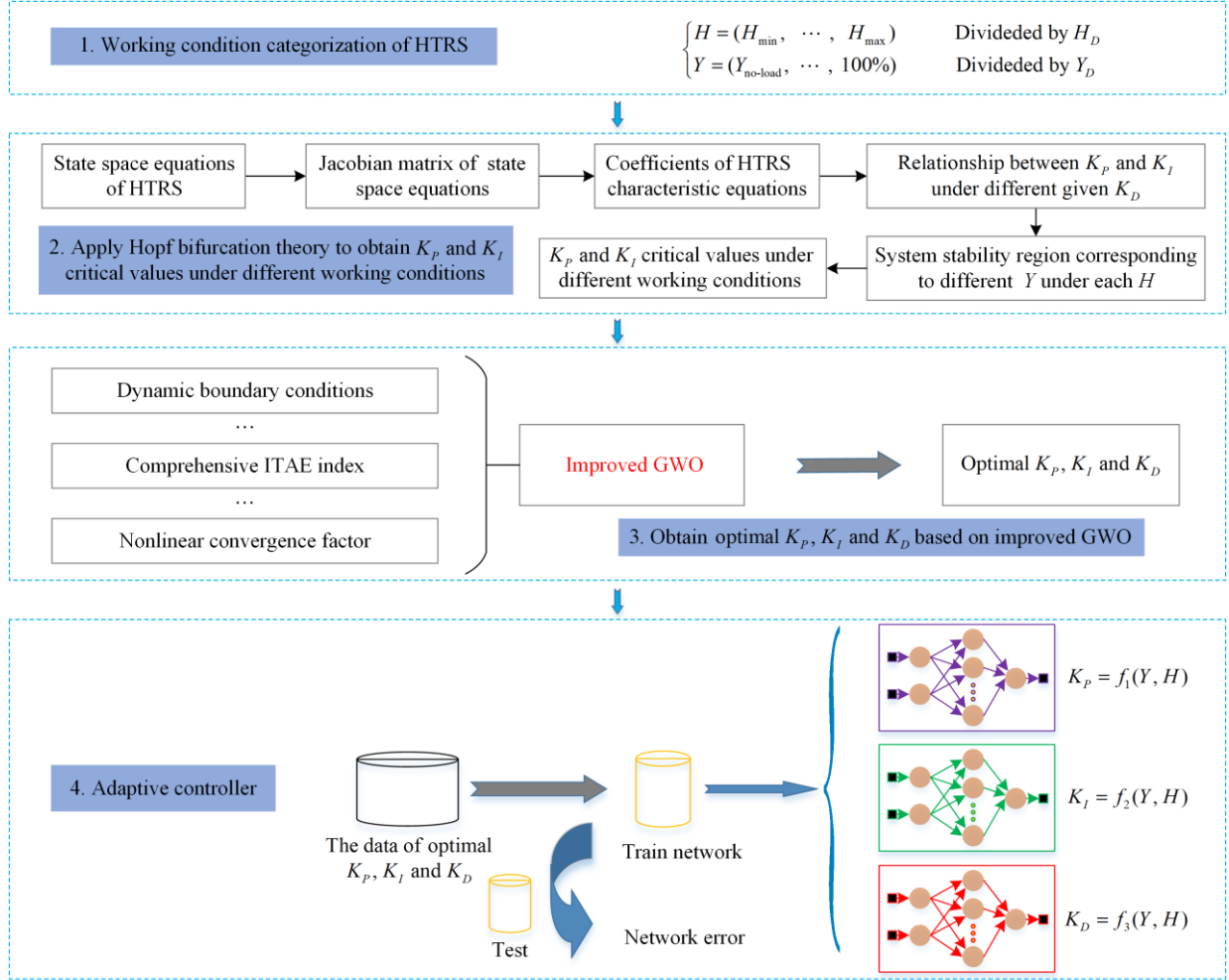
Fig. 5. Design process of V-PID controller.

A. Working Condition Categorization of HTRS

The training of the controller neural network requires a large amount of sample data, so it is necessary to categorize the working conditions. Since the HTRS is sensitive to H and Y, the categorization should be carried out according to H, Y, and the accuracy requirements of the controller neural network. Thus, H_D is used as the smallest unit to divide H, and Y_D is used as the smallest unit to divide Y from the actual no-load opening to 100% opening with different H. It is worth noting that although the amount of no-load opening data of a hydropower station is generally limited, an intelligent algorithm can be used to obtain the relationship between the no-load Y and H through parameter identification, so as to obtain the no-load Y with different H.

B. Determination of Critical Values of Controller Parameters

The critical values of the controller parameters are determined by the Hopf bifurcation theory.

1) Stability Constraints

For the *n*-order nonlinear system $\dot{x} = f(x, v)$, where $x \in R^n$ is the state vector and $v \in R^1$ is the unknown parameter [6], the characteristic equation of the Jacobian matrix of the system at the equilibrium point (x_0, v_0) is given as [31]:

$$F(\lambda, v) = \sum_{i=0}^{n} p_i(v)\lambda^i = 0 \qquad (15)$$

where λ is the root of the characteristic equation; p_i is the coefficient of the characteristic equation. It is related to the system parameters.

According to the Hopf bifurcation theory [32], for a nonlinear dynamic system, when the system is critically stable, the characteristic equation has two eigenvalues whose real part is 0 (i.e., a pure imaginary conjugate complex root), and (n-2) real roots whose parts are not 0. Therefore, the characteristic polynomial of the system satisfies:

$$F(\lambda) = (\lambda^2 + w^2)\left(\lambda^{n-2} + \sum_{i=0}^{n-3} a_i \lambda^i\right) \qquad (16)$$

where w is the pure imaginary conjugate complex root; and a_i is the coefficient of other polynomials composed of characteristic roots with non-zero real parts.

Combining (15) and (16), all eigenvalues and unknown parameters that satisfy the critical stability conditions of the system can be determined.

2) System Stability Domain and the Critical Controller Parameters

The state space equation method is adopted to calculate the stable domain of the HTRS. The derivation process under PCM follows the steps [33]:

1) Obtain the differential equations of each subsystem according to (6), (9), and Fig. 3, expressed as:

$$\dot{y} = \frac{1}{T_y}(u - y) \qquad (17)$$

$$\dot{h} = -\frac{e_{qy}}{e_{qh}}\dot{y} - \frac{1}{e_{qh}T_w}h \qquad (18)$$

$$\dot{\omega}_G = \frac{1}{T_a}(m_t - m_e - K\omega_G) \qquad (19)$$

2) Obtain the differential equation of the controller, expressed as:

$$\begin{cases} u = K_P(p_c - m_t + \Delta f/\Delta e_p) + ix \\ ix = K_I(p_c - m_t + \Delta f/\Delta e_p) \end{cases} \qquad (20)$$

3) Integrate (17)–(20) to obtain the state space equation of the HTRS, expressed as:

$$\begin{cases} \dot{\omega}_G = \frac{1}{T_a}(m_t - m_e - K\omega_G) \\ \dot{y} = \frac{1}{T_y}\left[K_P(p_c - m_t + \Delta f/\Delta e_p) + ix - y\right] \\ \dot{h} = -\frac{e_{qy}}{e_{qh}}\dot{y} - \frac{1}{e_{qh}T_w}h \\ ix = K_I(p_c - m_t + \Delta f/\Delta e_p) \\ \dot{\varphi} = \omega_0\omega_G \end{cases} \qquad (21)$$

By analyzing the Jacobian matrix of (21), the relationship between characteristic root and PID control parameters is determined when the HTRS is critically stable, and then the constraint function of controller parameters $K_I = f(K_P)$ can be obtained, as shown in (22). The system stability domain and the boundary values of the controller parameters are also obtained.

$$K_I = \frac{a_1 K_P^2 + a_2 K_P + a_3}{b_1 K_P + b_2} \qquad (22)$$

where a_1, a_2, a_3, b_1 and b_2 are the coefficients of the constraint function of controller parameters.

C. Acquisition of Optimal PID Parameters with Improved GWO

The wolves of the GWO are divided into four levels according to their fitness values, which satisfy: $\alpha > \beta > \delta > \omega$ [34]–[36]. In the hunting process of wolves, α, β, and δ guide the hunting behavior, while ω follows the first three wolves to besiege the prey. The position of the prey is equivalent to the solution of the problem to be optimized [37], [38]. The predation behavior of gray wolves includes encircling, hunting, and attacking prey [39]. The attack of wolves refers to the process of obtaining the optimal solution by the GWO [40], [41]. When attacking prey, the convergence factor m plays the role of adjusting the local optimization and global search, expressed as:

$$m = 2 - \frac{2t}{t_{max}} \qquad (23)$$

where t is the current number of iterations; and t_{max} is the maximum number of iterations.

However, the complex search process of the GWO makes the strategy of linearly decreasing the convergence factor m difficult to reflect the actual optimization process. Thus, to make m decrease nonlinearly in the specified interval, this paper adopts an iterative formula of m based on the exponential function [3], defined as:

$$m(t) = m_{initial}\left[1 - \left(\frac{t}{t_{max}}\right)^\mu\right] \qquad (24)$$

where $m_{initial}$ represents the initial value of m, which is taken as 2; while μ is the exponential adjustment factor, which is taken as 1.5.

To prove the advantages of the GWO in parameter optimization and the rationality of improving the iteration coefficient m, the particle swarm optimization (PSO) [10], biogeographical-based optimization (BBO) [42], and gravitation search (GSA) [13], and GWO with linearly adjusted m and GWO with nonlinearly adjusted m (NGWO) algorithms are compared and analyzed through four commonly used benchmark functions [43]. Table I and Figure 6 show the mathematical descriptions and the three-dimensional surface diagrams of the four test functions, respectively. It can be seen that the Sphere is a unimodal function with only one global minimum. The Griewank is a multimodal function with multiple local optimal solutions, and it is difficult to find its global extremum because of the small difference of function values corresponding to the optimal solutions. The Resenbrock is a unimodal function, whose global extremum is also difficult to find because of the inter-

action between the variables. The Rastrigin has multiple local optimal solutions, but the function values of these optimal solutions differ greatly. Therefore, for the parameter optimization problem with multiple local opti- mal solutions which largely differ from the global optimal solution, the Rastrigin function can well test the optimization algorithms. Table II shows the parameter settings of the optimization algorithms.

TABLE I
MATHEMATICAL DESCRIPTIONS OF FOUR BENCHMARK FUNCTIONS

Benchmark functions	Function descriptions	Definition domain
Sphere	$F_1(x) = \sum_{i=1}^{n} x_i^2$	$[-20,\ 20]^n$
Griewank	$F_2(x) = \dfrac{1}{4000} \sum_{i=1}^{n} x_i^2 - \prod_{i=1}^{n} \cos\left(\dfrac{x_i}{\sqrt{i}}\right) + 1$	$[-300,\ 300]^n$
Rosenbrock	$F_3(x) = \sum_{i=1}^{n-1} (100(x_{i+1} - x_i^2)^2 + (x_i - 1)^2)$	$[-10,\ 10]^n$
Rastrigin	$F_4(x) = \sum_{i=1}^{n} (x_i^2 - 10\cos(2\pi x_i) + 10)$	$[-5.12,\ 5.12]^n$

TABLE II
INITIALIZATION PARAMETERS OF OPTIMIZATION ALGORITHMS

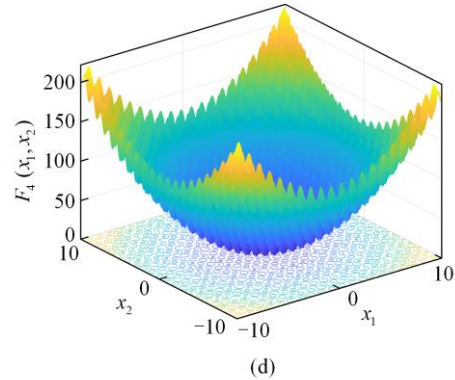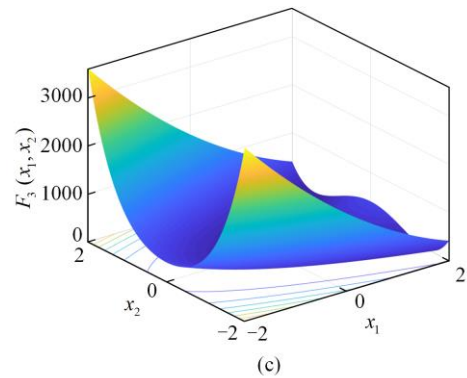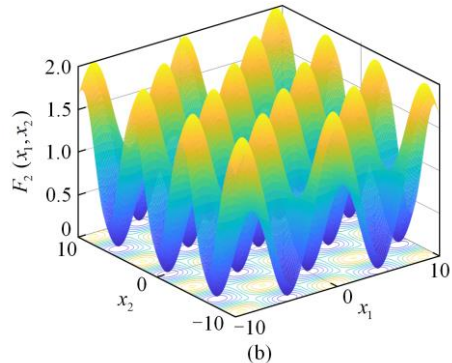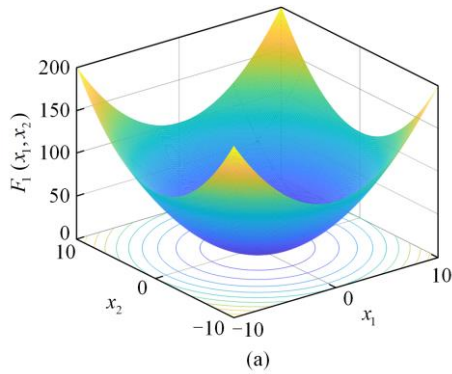| Optimization algorithm	Population size	Iterations	Initial parameter setting
PSO	30	2000	Initial weight $w = 0.8$, learning rate $c_1 = c_2 = 1.5$
BBO	30	2000	Probability of variation $P_m = 0.01$, retention ratio $R_k = 0.2$
GSA	30	2000	Gravitational constant $G_0 = 100$, decay rate $\beta_0 = 20$
GWO	30	2000	Iteration coefficient $m_{initial} = 2$
NGWO	30	2000	Iteration coefficient $m_{initial} = 2$

Fig. 6. Three-dimensional surface diagrams of the four benchmark functions. (a) Sphere. (b) Griewank. (c) Rosenbrock. (d) Rastrigin.

Figure 7 shows the change curves of the average fitness of different algorithms in logarithmic form (100 tests). As seen, the average fitness of GWO and NGWO decreases sharply and reaches a lower value, indicating their high accuracy compared to the other optimization algorithms. In addition, it can be seen from Fig. 7(d) that NGWO has a faster convergence rate than GWO. Therefore, NGWO is selected to deal with the parameter optimization problems with multiple local optimal solutions differing significantly from the global optimal solution. This is consistent with the parameter optimization problem with the specific target of the HTRS controller.

In addition, to improve the performance of the NGWO, this paper makes the following improvements.

1) Prey location boundary conditions

The position vector $S_p(t)$ of the prey in the tth generation corresponds to the K_P, K_I, and K_D values of the controller studied in this paper. In order to reduce the simulation calculation time, the boundary values of K_P, K_I, and K_D included in $S_p(t)$ are adjusted in real-time according to the system stability domain in different working conditions.

Fig. 7. Change curves of the average fitness of different algorithms. (a) Average fitness of Sphere. (b) Average fitness of Griewank. (c) Average fitness of Rosenbrock. (d) Average fitness of Rastrigin.

2) Fitness function

In the PID parameter optimization, the fitness function primary adopts the standard ITAE [44], [45] index (J_{ITAE}), i.e., the absolute value of the error multiplied by the time integral, expressed as:

$$J_{\text{ITAE}} = \int_0^{t_s} t\left|e(t)\right| \mathrm{d}t \tag{25}$$

where t is the current simulation time; t_s is the total simulation time; and $e(t)$ is the error integral of hydro-turbine mechanical power.

To avoid excessive overshoot σ_1, reverse adjustment σ_2 and long adjustment time t_r, σ_1, σ_2, and t_r are used as part of the objective function to form a comprehensive ITAE index $(J_{\text{COM-ITAE}})$, expressed as:

$$J_{\text{COM-ITAE}} = \int_0^{t_s} t\left|e(t)\right| \mathrm{d}t + \omega_1 \mathrm{e}^{\sigma_1} + \omega_2 \mathrm{e}^{\sigma_2 + 0.002} + \omega_3 t_r \tag{26}$$

where ω_1, ω_2, and ω_3 are the adjustment coefficients of σ_1, σ_2, and t_r, respectively. To determine the suitable values of ω_1, ω_2, and ω_3, 7 schemes are taken for comparison, whose parameters are shown in Table III, and the comparison results are shown in Fig. 8. As can be seen from Fig. 8, σ_2 and t_r of the 7 schemes have minor differences, while σ_1 in Scheme 1 is smaller than that in other schemes. Therefore, σ_1, σ_2, and t_r are taken as 1, 1, and 0.2, respectively.

TABLE III
ADJUSTMENT COEFFICIENTS OF EACH SCHEME

Coefficients	Scheme 1	Scheme 2	Scheme 3	Scheme 4	Scheme 5	Scheme 6	Scheme 7
ω_1	1	10	100	1	1	1	1
ω_2	1	1	1	10	100	1	1
ω_3	0.2	0.2	0.2	0.2	0.2	2	20

For the improved NGWO (INGWO), the controller parameters are optimized for the HTRS in different working conditions, i.e., the sample data for the training of the controller neural network is obtained.

(a)

(b)

(c)

(d)

(e)

(f)

Fig. 8. Comparison results of adjustment coefficients. (a) $H = H_r$, $Y = 30\%$. (b) $H = H_{\min}$, $Y = 90\%$. (c) $H = H_r$, $Y = 30\%$. (d) $H = H_r$, $Y = 90\%$. (e) $H = H_{\max}$, $Y = 30\%$. (f) $H = H_{\max}$, $Y = 90\%$.

Figure 9 shows the calculation procedure of the optimal controller parameters in the given conditions, where the initialization parameters of INGWO are: population size $N_P = 30$, iterations $N_I = 100$, $m_{\text{initial}} = 2$, and $\mu = 1.5$.
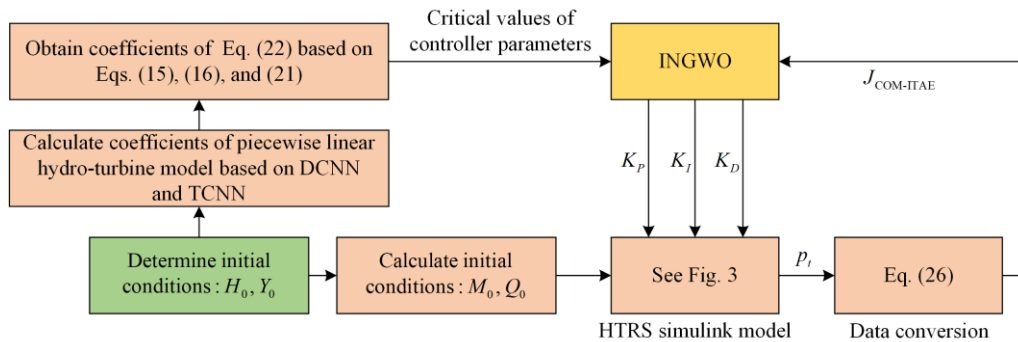
Fig. 9. Calculation procedure of optimal controller parameters under given conditions.

D. V-PID Controller Structure

Both single and multiple neural networks are available for the V-PID controller. For the single neural network, the input is composed of Y and H, and the output is composed of K_P, K_I, and K_D, whereas for the multiple neural networks, the input is composed of Y and H, and the output is K_P, K_I, or K_D. In addition, the number of neurons in the hidden layer (N_h) of the neural network is vital and is generally selected according to (27) [46]. To determine the appropriate value of N_h, the maximum N_h is determined by adopting (27), and then the sensitivity analysis of N_h is conducted as shown in Fig. 10. As seen, for the multiple neural networks, M_{SE} of K_P is smaller when N_h is 8 or 11, and M_{SE} of K_I is smaller when N_h is larger than 7. For the single neural network, M_{SE} of K_P and K_I is smaller when N_h is larger than 7. Considering that too many neurons in the hidden layer can easily make the network overfit, N_h is selected as 8 for both single and multiple neural networks.

$$N_h < \sqrt{N_i + N_o} + Z \qquad (27)$$

where N_i is the number of neurons in the input layer; N_o is the number of neurons in the output layer; and Z is a constant as [0,10].

To determine the reasonable structure of the V-PID neural network, an actual hydropower station is used as an example to conduct the test. The hydropower station under PCM adopts the PI-type control method. Therefore, the neural network with 2 inputs and 2 outputs (scheme 1: 2-8-2 neural network structure) and neural networks with 2 inputs and 1 output (scheme 2: 2-8-1 neural network structure) are trained and compared respectively. The error comparison is shown in Fig. 11. The determination coefficient (R^2) and the root mean square error (R_{MSE}) are used as the evaluation criteria for the two schemes [47], [48]. The larger the R^2 and the smaller the R_{MSE}, the better the network fitting effect. The formulas for calculating R^2 and R_{MSE} are given as:

Fig. 10. Sensitivity analysis results of N_h. (a) Single neural network. (b) Multiple neural networks.
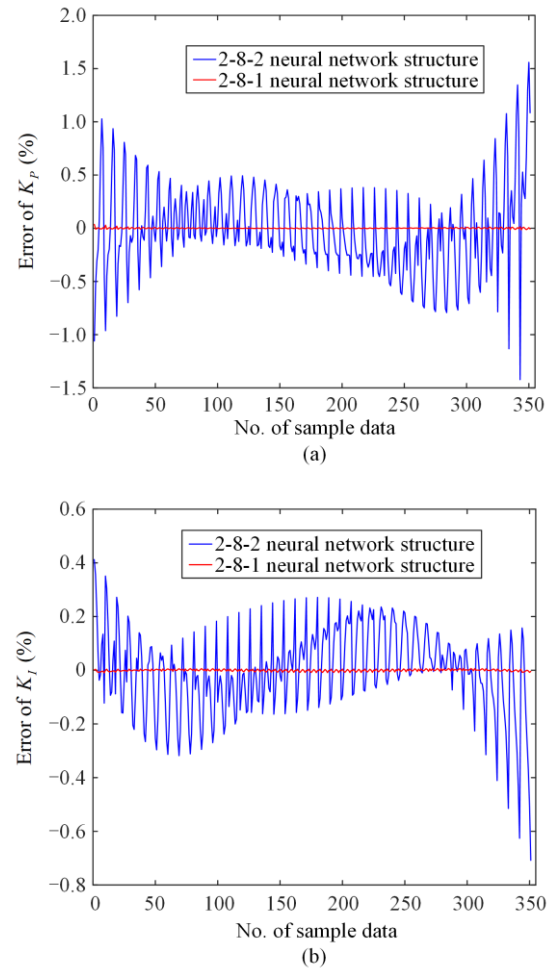
Fig. 11. Comparison of prediction errors of controllers in two structures. (a) Comparison of K_p errors. (b) Comparison of K_I errors.

$$R^2 = 1 - \frac{\sum_{i=1}^{n}(d_i - K_i)^2}{\sum_{i=1}^{n}(d_i - \bar{d})^2} \qquad (28)$$

$$R_{\text{MSE}} = \sqrt{\frac{\sum_{i=1}^{n}(d_i - K_i)^2}{n}} \qquad (29)$$

where d_i represents K_P or K_I sample data; K_i represents K_P or K_I prediction data; n represents the number of sample data; and $\bar{d}$ represents the mean of K_P or K_I sample data.

The calculation results for the error comparison are shown in Table IV. As shown, scheme 2 has a smaller error and higher reliability than scheme 1. Thus, the structure of the V-PID controller neural networks with 2 inputs and 1 output is determined, as shown in Fig. 12, where K_P, K_I, and K_D automatically update based on H and Y in the "Save" module and satisfy (30)–(32), while H and Y are in the "Save" update only when $\Delta p \geqslant p_\varepsilon$. $p_\varepsilon = 0.005$ is adopted. Since the regulation

of the controller is controlled by the oil pressure, it is necessary to determine an appropriate value through real machine tests when used in actual production to balance the speed and accuracy of the controller. Accordingly, when $\Delta p \geqslant 0.005$ within a certain period of time, the controller neural networks act and output new PID parameters. From [6], it is feasible for the neural networks to implement in hardware form, so the designed controller has great application value.

$$K_P = f_1(Y, H) \qquad (30)$$
$$K_I = f_2(Y, H) \qquad (31)$$
$$K_D = f_3(Y, H) \qquad (32)$$

TABLE IV
COMPARISON OF PARAMETER PREDICTION RESULTS OF
CONTROLLERS IN TWO STRUCTURES

Structure type	Data type	R_{MSE}	R^2
2 inputs and 1 output	K_P	4.46×10^{-5}	1
	K_I	1.23×10^{-5}	1
2 inputs and 2 outputs	K_P	0.009 3	0.997 6
	K_I	0.001 8	0.999 4
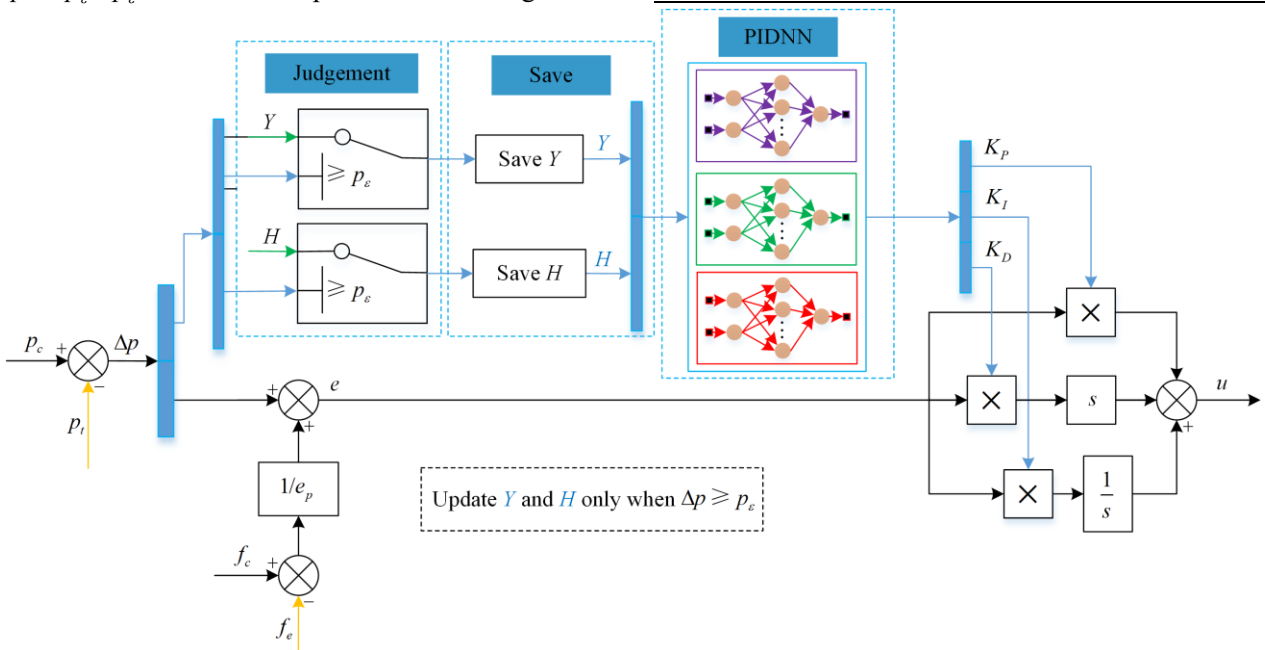
Fig. 12. Structure of V-PID controller under PCM based on neural networks.

IV. SIMULATION TEST VERIFICATION AND RESULT ANALYSIS

To verify the effect of the V-PID controller, a simulation test, which takes a Francis hydropower station in the southwest of China (XLD) as an example, is carried out. The system parameters of the hydropower station under PCM are shown in Table V. The data used in the turbine modeling and the modeling effects are shown in Appendix A and B, respectively, while the detailed data of the diversion pipeline is shown in Appendix C. Based

on the data of the XLD hydropower station, the nonlinear HTRS simulation platform is constructed, and then $H_D = 2$ m and $Y_D = 10\%$ are used to categorize working conditions, while INGWO is used to obtain the optimal PID parameters in different working conditions. Considering $K_D = 0$ under PCM, the PID neural network contains K_P and K_I neural networks. Therefore, K_P and K_I neural networks are trained respectively after obtaining the optimal PID parameters, and then the V-PID controller model based on BPNN is constructed.

Figure 13 shows the comparison between the training data and the prediction data of the V-PID neural networks, while Fig. 14 shows the fitting surfaces of the optimal controller parameter. As seen, the prediction error of the PID neural networks is small and the fitting accuracy is high, which can well represent the change of the optimal control parameters as the working conditions change. The stability proof of the V-PID controller is shown in Appendix D.

TABLE V
SYSTEM PARAMETERS OF HTRS

Subsystems	Parameters
Controller	$e_p = 0.04$, $b_p = 0.01$, $K_P = 0.28$, $K_I = 0.2$, and $K_D = 0$
Servo system	$T_y = 0.459$
Diversion system	$T_w = 0.873$
Generator and load	$T_a = 12.239$, $K = 0$, $\omega_0 = 314$, $X_r = 125$, $e_g = 0.176$
Hydro-turbine	$D = 6.223\,\mathrm{m}$, $H_r = 197\,\mathrm{m}$, $H_{\max} = 229.4\,\mathrm{m}$, $H_{\min} = 154.6\,\mathrm{m}$, $Q_r = 432.7\,\mathrm{m^3/s}$
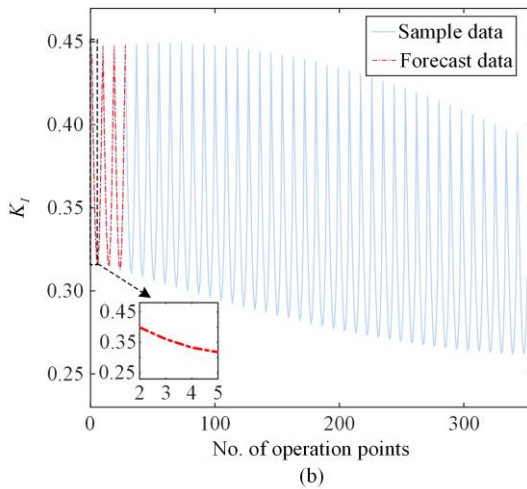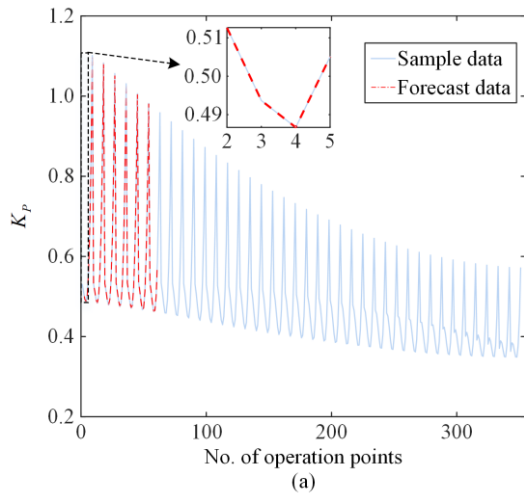
Fig. 13. Prediction effect of V-PID neural network. (a) Prediction effect of K_p. (b) Prediction effect of K_I.
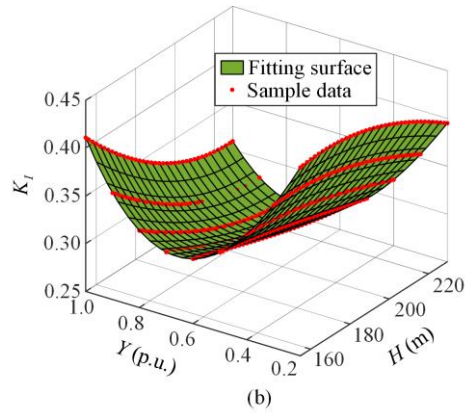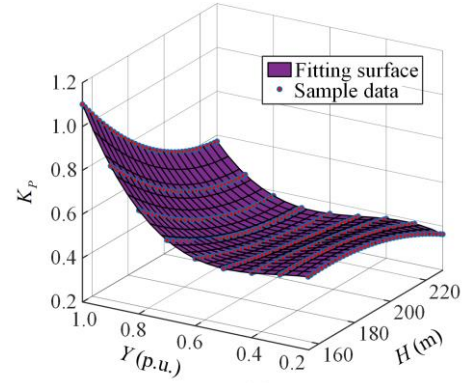
Fig. 14. Neural network fitting effect of V-PID controller. (a) Neural network fitting effect of K_p. (b) Neural network fitting effect of K_I.

Finally, $Y = 30\%$ and 90% are selected as the simulation operating points with $H_{\min}$, H_r, and $H_{\max}$ respectively to verify the superiority of the proposed neural network-based V-PID controller over the traditional F-PID controller, the generalized predictive controller (GPC) without noise input, the PID predictive controller based on BPNN online training (OTV-PID). Among these controllers, the linear hydro-turbine model is adopted only when GPC is used. Table VI shows the key parameters of the GPC and OTV-PID controllers. The selection mode of working conditions corresponds to a representative large span of H and Y. The test results of each working point are shown in Fig. 15, where M_{ref} is the reference value of M_t. As seen, GPC generates large oscillation during online training despite the ideal condition of no noise interference, indicating its poor control effect. For OTV-PID, t_r is more than 65 s because of the continuous adjustment of the weight and threshold in a longer online training time. The difference of σ_2 between the F-PID and the V-PID controller models is small in different working conditions, while compared with the traditional F-PID, the setting and rise times of the V-PID controller are shorter. In addition, although the overshoot of the V-PID controller is relatively large, M_t oscillates only once, meeting the requirements of the engineering application.

TABLE VI
PARAMETERS OF GPC AND OTV-PID CONTROLLERS

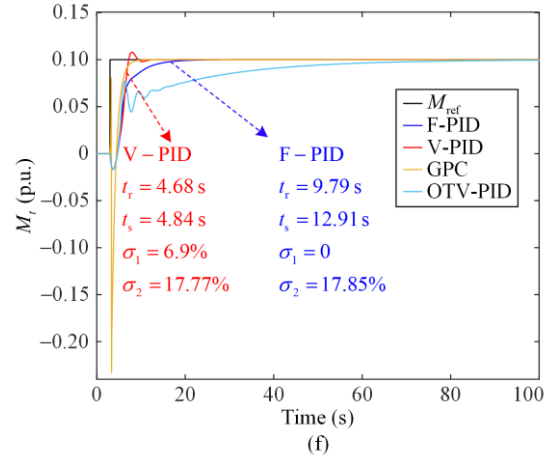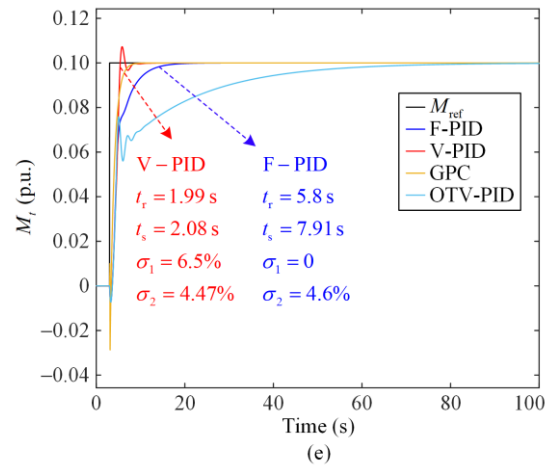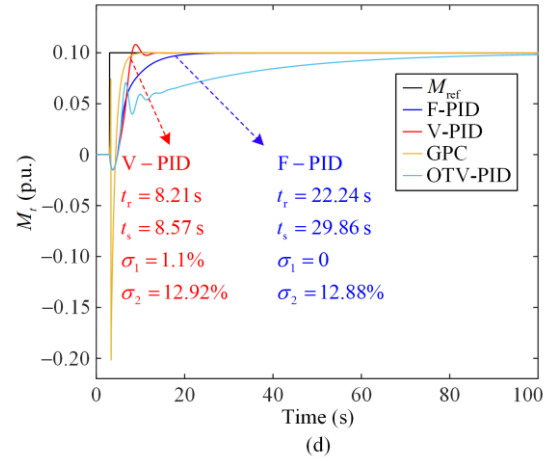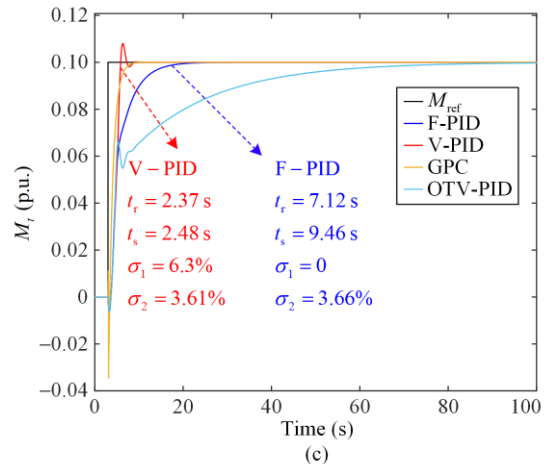| Controller	Parameters
GPC	Minimum output length $N_1 = 1$, predicted length $N = 60$, input delay $d = 1$, control length $N_u = 10$, output softening coefficient $S_c = 0.99$
OTV-PID	No. of the neurons in input-layer $N_{in} = 3$, No. of the neurons in hidden-layer $N_h = 5$, No. of the neurons in output-layer $N_{out} = 3$, learning rate $L_r = 0.2$, inertia coefficient $I_c = 0.05$

(a)

(b)

(c)

(d)

(e)

(f)
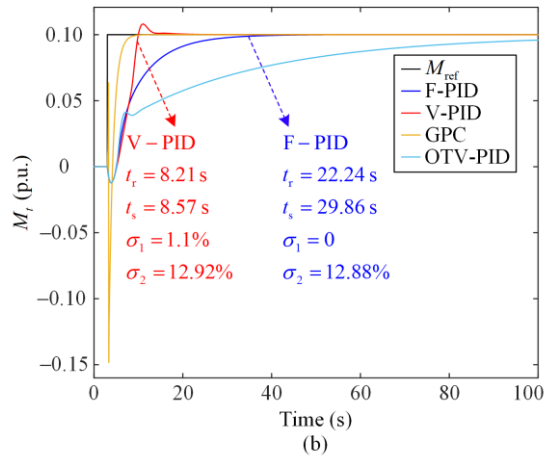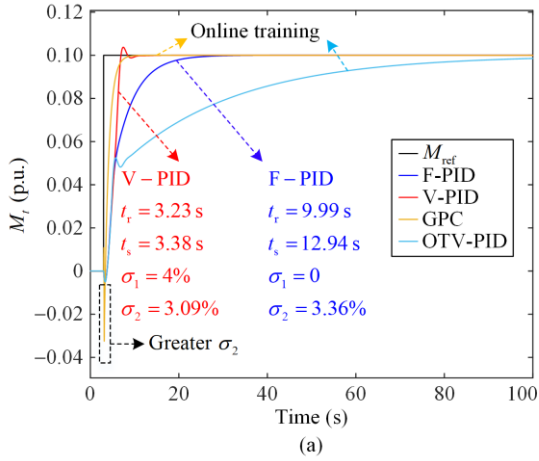
Fig. 15. Simulation comparison test results. (a) $H = H_{min}, Y = 30\%$. (b) $H = H_{min}, Y = 90\%$. (c) $H = H_r, Y = 30\%$. (d) $H = H_r, Y = 90\%$. (e) $H = H_{max}, Y = 30\%$. (f) $H = H_{max}, Y = 90\%$.

From the perspective of practical application, the V-PID controller brings multiple benefits to the power grid by reducing the adjustment time of the HTRS in full working conditions. First, shorter regulation time means that the power system can respond more quickly to load changes, thereby improving the stability and robustness of the power grid. Second, the faster re-

sponse of HTRS can be more effective in maintaining the frequency and voltage levels of the power grid, ensuring normal operation of the power system. In addition, improving the performance of the HTRS can also help reduce the dependence of the power grid on backup power generation equipment, thereby improving the reliability and sustainability of the power grid. Shorter regulation time can also reduce unstable factors in the power system. This helps to reduce the operational risks of the system. Therefore, the V-PID controller can have a positive impact on the stability, reliability, and overall performance of the power grid.

V. CONCLUSION

Taking the prototype turbine test data and actual operational data as the sample data, this paper uses the GWO to modify the prototype turbine test data and constructs a high-precision turbine model based on BPNN and a nonlinear HTRS simulation platform. Hopf bifurcation theory is adopted to calculate the stable domain of HTRS in typical working conditions to improve the GWO and obtain the optimal PID parameters efficiently. In addition, taking the optimal PID parameters in typical working conditions as sample data, the neural networks of V-PID controllers with different structures are trained, and a V-PID controller with good structure, small error, and high reliability is obtained. The proposed offline training and online adaptation-based V-PID controller only adds three modules of 'Judgment', 'Save', and 'PIDNN' to the structure, which not only greatly reduces the rise and regulation times, but also realizes optimal control of the hydropower unit in full working conditions. The proposed controller provides an effective improved solution for the governing controller of hydropower units.

However, the construction of the V-PID controller relies on an accurate HTRS model and is thus not suitable for hydropower stations where it is difficult to obtain enough modeling data. This paper theoretically studies the offline training and online adaptation-based V-PID controller considering the nonlinearity of the hydro-turbine while the nonlinearity of the diversion system is ignored. In the future, theoretical research and experimental verification will be conducted on the V-PID controller that considers the nonlinearities of both the diversion system and the hydro-turbine.

APPENDIX A

A. Experimental and Test Data for the Modeling of Hydro-turbine

To ensure the accuracy of the hydro-turbine model, the test and operational data at multiple water heads of an actual hydropower plant are used. The test data is provided by the turbine manufacturer, as shown in Fig. A1.

The operational data are obtained from the monitoring system shown in Fig. A2, with a sampling time of 0.01 s.
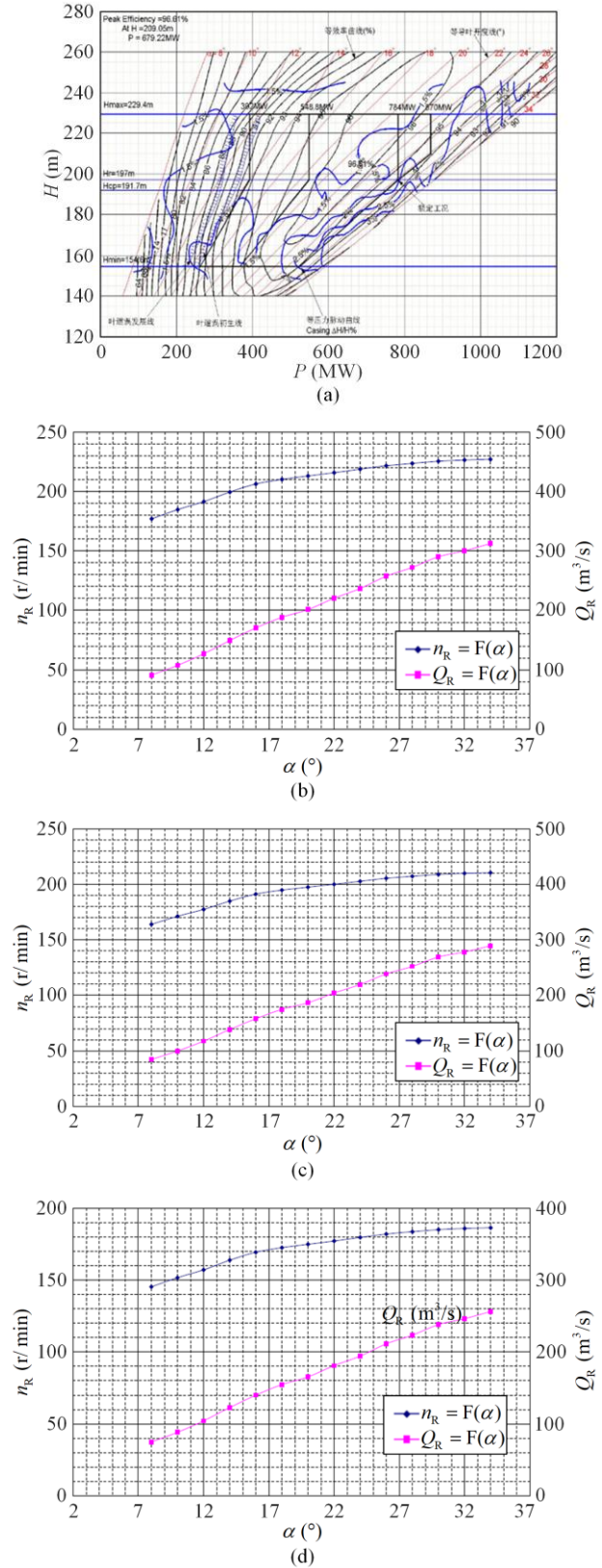

Fig. A1. Hydro-turbine test data. (a) Test data at operating conditions. (b) Runaway data when $H = H_{max}$. (c) Runaway data when $H = H_r$. (d) Runaway data when $H = H_{min}$.
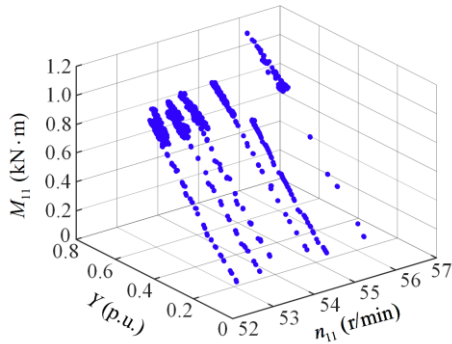
Fig. A2. Hydro-turbine operational data.

APPENDIX B

B. Effect of Hydro-turbine Modeling

The change of loss function during the iteration process is shown in Fig. B1, the actual modeling error is shown in Fig. B2, and the discharge and torque characteristic surfaces are shown in Fig. B3. Taking TCNN as an example, the comparison with the actual operational data is shown in Fig. B4.
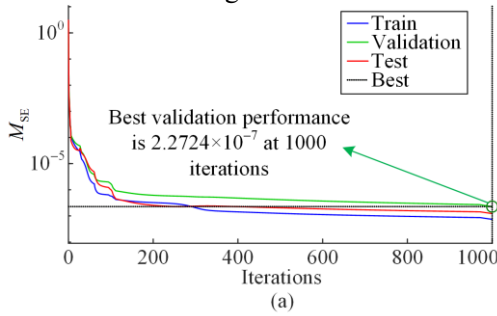

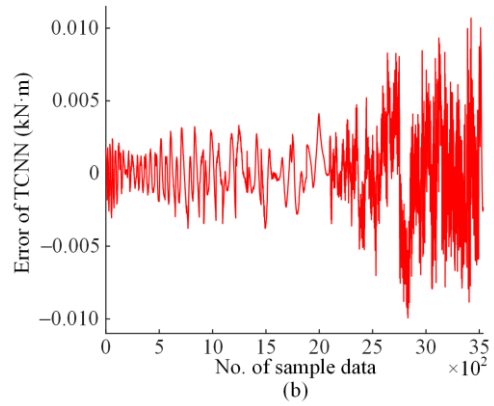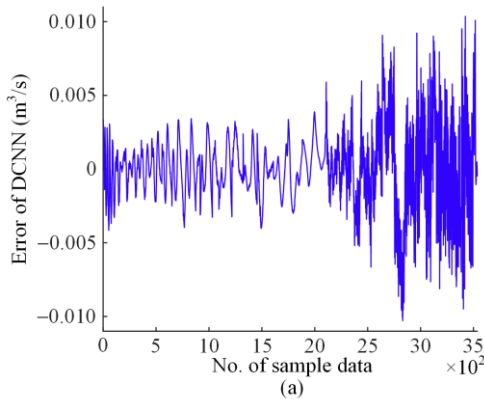Fig. B1. Iteration process of hydro-turbine model. (a) The iteration process of DCNN. (b) The iteration process of TCNN.

Fig. B2. Actual modeling error of hydro-turbine. (a) Modeling error of DCNN. (b) Modeling error of TCNN.
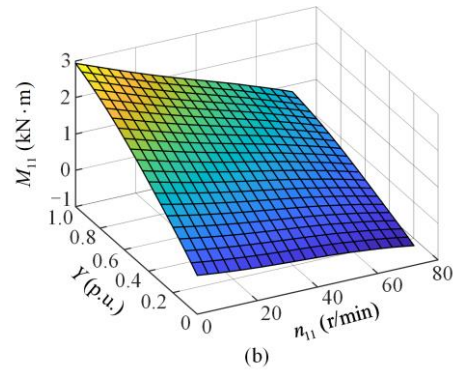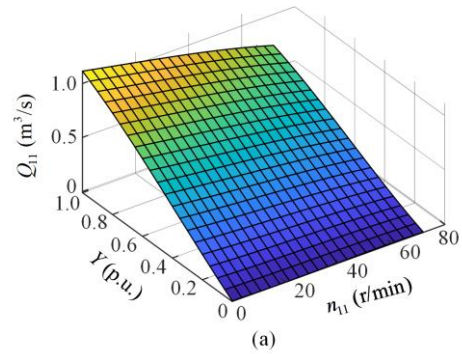
Fig. B3. Fitting surfaces of DCNN and TCNN. (a) Discharge characteristic fitting surface. (b) Torque characteristic fitting surface.
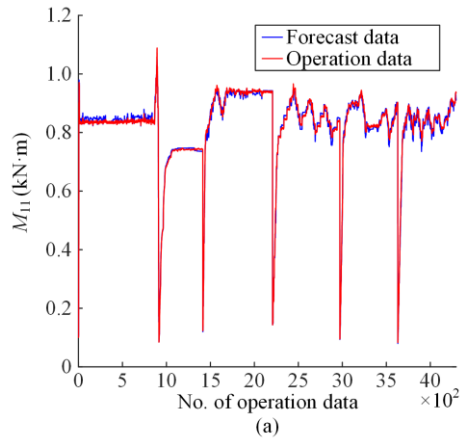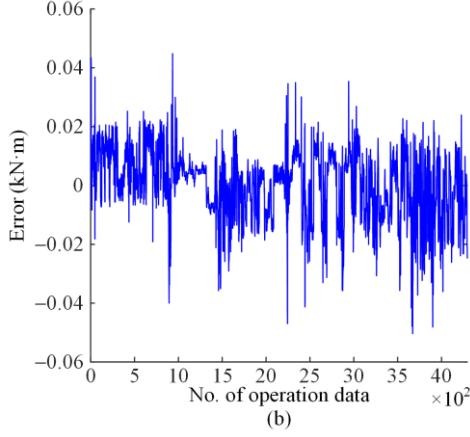
Fig. B4. Verification result of hydro-turbine TCNN. (a) Following effect of TCNN. (b) Following error of TCNN.

APPENDIX C

C. Detailed Data of the Diversion Pipeline

The planning diagram of the diversion pipeline [3] between the reservoir and the hydro-turbine volute is shown in Fig. C1.
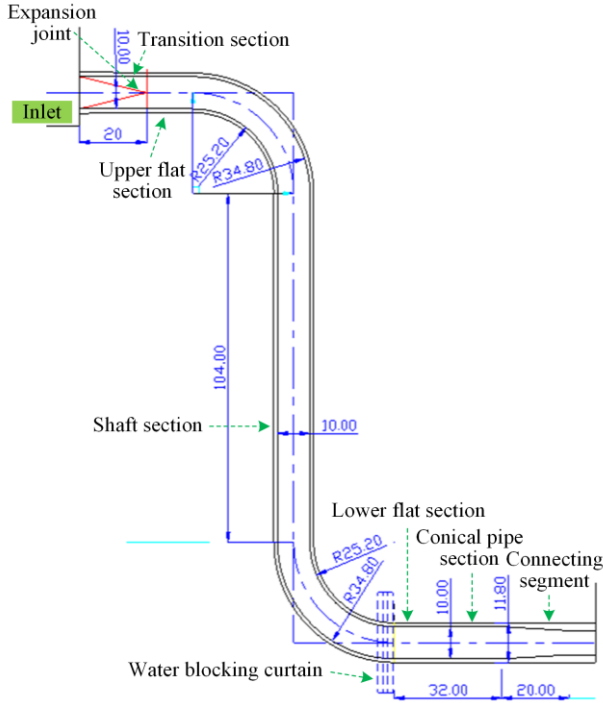
Fig. C1. Planning diagram of the diversion pipeline.

APPENDIX D

D. Stability Proof of V-PID Controller

Let $x_1 = \omega$, $x_2 = y$, $x_3 = h$, $x_4 = ix$, $x_5 = \varphi$, the state equation of HTRS can be obtained, and is based on (21) and expressed as:

$$
\begin{cases}
\dot{x}_1 = \dfrac{1}{T_a}\left(m_t - m_e - Kx_1\right) \\[2mm]
\dot{x}_2 = \dfrac{1}{T_y}\left[K_P\left(p_c - m_t + \Delta f / \Delta e_p\right) + ix - x_2\right] \\[2mm]
\dot{x}_3 = -\dfrac{e_{qy}}{e_{qh}}\dot{x}_2 - \dfrac{1}{e_{qh}T_w}x_3 \\[2mm]
\dot{x}_4 = K_I\left(p_c - m_t + \Delta f / \Delta e_p\right) \\[2mm]
\dot{x}_5 = \omega_0 x_1
\end{cases} \tag{33}
$$

Equation (33) can be simplified as:

$$
\dot{x} = f(x) \tag{34}
$$

where x is a 5-dimensional state vector; and f is a nonlinear vector function with the same dimension as x.

Assuming that the origin $x_e = 0$ is in an equilibrium state and $f(x)$ is differentiable for x_i ($i = 1 - 5$), the Jacobian matrix of HTRS can be expressed as (35).

$$
J(x) = \frac{\partial f(x)}{\partial x} = \begin{pmatrix}
\dfrac{\partial f_1}{\partial x_1} & \dfrac{\partial f_1}{\partial x_2} & \cdots & \dfrac{\partial f_1}{\partial x_5} \\[2mm]
\dfrac{\partial f_2}{\partial x_1} & \dfrac{\partial f_2}{\partial x_2} & \cdots & \dfrac{\partial f_2}{\partial x_5} \\[2mm]
\vdots & \vdots & & \vdots \\[2mm]
\dfrac{\partial f_5}{\partial x_1} & \dfrac{\partial f_5}{\partial x_2} & \cdots & \dfrac{\partial f_5}{\partial x_5}
\end{pmatrix} =
$$

$$
\begin{pmatrix}
-\dfrac{K}{T_a} & -\dfrac{e_y}{T_y} & -\dfrac{e_h}{T_y} & 0 & 0 \\[3mm]
0 & \dfrac{-1 - K_P e_y}{T_y} & \dfrac{-K_P e_h}{T_y} & \dfrac{1}{T_y} & 0 \\[3mm]
0 & \dfrac{e_{qy}}{e_{qh}}\dfrac{1 + K_P e_y}{T_y} & \dfrac{e_{qy}}{e_{qh}}\dfrac{K_P e_h}{T_y} - \dfrac{1}{e_{qh}T_w} & -\dfrac{e_{qy}}{e_{qh}T_y} & 0 \\[3mm]
0 & -K_I e_y & -K_I e_h & 0 & 0 \\[3mm]
\omega_G & 0 & 0 & 0 & 0
\end{pmatrix} \tag{35}
$$

The sufficient condition for the asymptotic stability of HTRS at the origin is that (36) is positive definite as for a positive definite real symmetry P, and (37) is its Lyapunov function [49].

$$
Q(x) = -\left[J^T(x)P + PJ(x)\right] \tag{36}
$$

$$
V(x) = \dot{x}^T P\dot{x} = f^T(x)Pf(x) \tag{37}
$$

If there is $V(x) \to \infty$ when $\|x\| \to \infty$, the HTRS is globally asymptotically stable at $x_e = 0$.

Proof. Selecting the quadratic function shown in (38) as a Lyapunov function, then $V(x)$ is positive definite.

$$
V(x) = x^T P\dot{x} = f^T(x)Pf(x) \tag{38}
$$

where P is a positive definite symmetric matrix.

Considering that $f(x)$ is an explicit function of x rather than time t, there is:

$$
\frac{df(x)}{dt} = \dot{f}(x) = \frac{\partial f(x)}{\partial x}\frac{\partial x}{dt} = \frac{\partial f(x)}{\partial x}\dot{x} = J(x)f(x) \tag{39}
$$

Taking the full derivative of $V(x)$ over t along the state trajectory, $\dot{V}(x)$ can be obtained as:

$$\dot{V}(x) = f^T(x)P\dot{f}(x) + \dot{f}^T(x)Pf(x) =$$
$$f^T(x)PJ(x)f(x) + [J(x)f(x)]^T Pf(x) = \quad (40)$$
$$f^T(x)[J^T(x)P + PJ(x)]f(x)$$

$$\dot{V}(x) = -f^T(x)Q(x)f(x) \quad (41)$$

where $Q(x) = -[J^T(x)P + PJ(x)]$.

According to (41), to make the HTRS asymptotically stable, $\dot{V}(x)$ must be negative definite, i.e., $Q(x)$ must be positive definite.

If there is $V(x) \to \infty$ when $\|x\| \to \infty$, the HTRS is globally asymptotically stable at $x_e = 0$.

According to the Proof, taking $P = I$ (I is the unit matrix), the sequential principal sub determinant $\Delta_i (i = 1 - 5)$ of $Q(x)$ under typical working conditions is calculated, and the results are shown in Fig. D1. As shown, $\Delta_i > 0$, indicating that $Q(x)$ is positively definite for $x \neq 0$ [50].

In addition, when $\|x\| \to \infty$, there is:

$$V(x) = f^T(x)f(x) = \left(-\frac{K}{T_a}x_1 - \frac{e_y}{T_y}x_2 - \frac{e_h}{T_y}x_3\right)^2 +$$
$$\left(\frac{-1-K_P e_y}{T_y}x_2 + \frac{-K_P e_h}{T_y}x_3 + \frac{1}{T_y}x_4\right)^2 + \quad (42)$$
$$\left(\frac{e_{qy}}{e_{qh}}\frac{1+K_P e_y}{T_y}x_2 + \left(\frac{e_{qy}}{e_{qh}}\frac{K_P e_h}{T_y} - \frac{1}{e_{qh}T_w}\right)x_3 - \frac{e_{qy}}{e_{qh}T_y}x_4\right)^2 +$$
$$(-K_I e_y x_2 - K_I e_h x_3)^2 + (\omega_G x_1)^2 \to \infty$$

Therefore, the HTRS is globally asymptotically stable at $x_e = 0$.
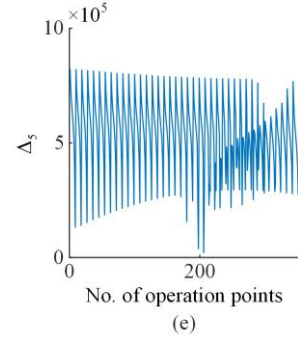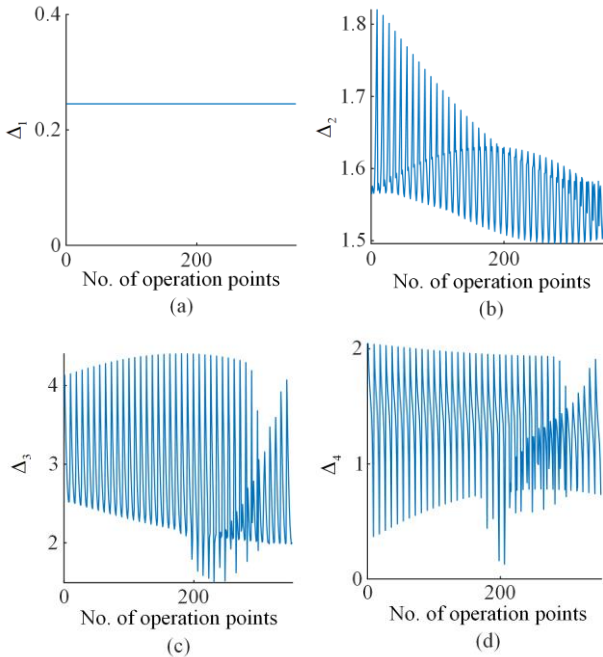
Fig. D1. Δ_i under typical working conditions. (a) Δ_1. (b) Δ_2. (c) Δ_3. (d) Δ_4. (e) Δ_5.

However, due to ignoring the nonlinearity of hydro-turbine, it is necessary to further study the proof method of V-PID stability. Therefore, combined with the characteristics of Lyapunov's second method [49], the stability judgment index (I_v), which is based on the integral value of the controlled variable in a period under the stable state as shown in (43), is adopted to prove the V-PID stability. For the stable system, $I_v = 0$ in theory. To reduce the calculation time, this paper takes the maximum simulation time $t_{max} = 50$ s, and the integration calculation time $t_{lim} = 10$ s. I_v in typical working conditions is shown in Fig. D2. As seen, $I_v = 0$ in each typical working condition, indicating that the stability of the V-PID controller meets the requirements.
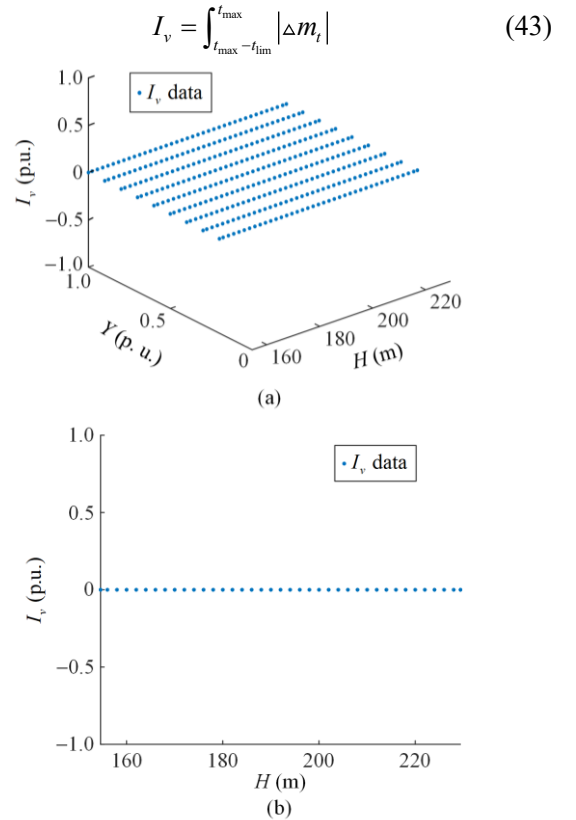
$$I_v = \int_{t_{max} - t_{lim}}^{t_{max}} |\Delta m_t| \quad (43)$$

(a)

(b)

Fig. D2. I_v under typical working conditions. (a) 3D perspective. (b) Plane perspective.

(a)

(b)

(c)

(d)

AUTHOR INFORMATION

Jinbao Chen graduated from the School of Power and Mechanical Engineering, Wuhan University, Wuhan, China. He is currently a scientific researcher at China Yangtze River Electric Power Co., Ltd., Wuhan, China. His research interest includes multidimensional modeling and advanced control of hydropower units.

Gang He received a bachelor's degree at the School of Electric Power, North China University of Water Resources and Hydropower, Zhengzhou, China. He is currently an engineer at Hebei Fengning Pumped Storage Co., Ltd., State Grid Xinyuan Company, Chengde, China. His research interest includes optimal control and hydraulic calculation of hydropower units.

Yunhe Wang received a bachelor's degree and a master's degree at the School of Power and Mechanical Engineering, Wuhan University, Wuhan, China. She is currently a Ph.D. student at School of Power and Mechanical Engineering, Wuhan University, Wuhan, China. Her research interest includes fault diagnosis and optimal control of hydropower units.

Yang Zheng graduated from the School of Hydroelectric and Digital Engineering, Huazhong University of Science and Technology, Wuhan, China. He is currently an associate researcher at the School of Power and Mechanical Engineering, Wuhan University, Wuhan, China. His research interest includes predictive control and hydraulic calculation of hydropower units.

Zhihuai Xiao graduated from the School of Power and Mechanical Engineering, Wuhan University, Wuhan, China. He is currently a professor at the School of Power and Mechanical Engineering, Wuhan University, Wuhan, China. His research interest includes fault diagnosis and optimal control of hydropower units.

REFERENCES

[1] D. Jiao, C. Z. Shao, and B. Hu et al., "Age-of-information-aware PI controller for load frequency control," Protection and Control of Modern Power Systems, vol. 8, no. 3, pp. 631-645, Nov. 2023.

[2] Y. Cao, S. Han, and N. Rong et al., "Dispatch of a cascade hydro-thermal-wind-photovoltaic-storage complementary system based on GCTMSA," Power System Protection and Control, vol. 51, no. 3, pp. 108-116, Feb. 2023. (in Chinese)

[3] J. Chen, Y. Zheng, and D. Liu et al., "Quantitative stability analysis of complex nonlinear hydraulic turbine regulation system based on accurate calculation," Applied Energy, vol. 351, p. 121853, 2023.

[4] M. M. Gulzar, "Designing of robust frequency stabilization using optimized MPC-(1+PIDN) controller for high order interconnected renewable energy based power systems," Protection and Control of Modern Power Systems, vol. 8, no. 1, pp. 180-193, Jan. 2023.

[5] J. Chen, G. Ren, and Q. Ding et al., "Study on a quantitative stability analysis method of a hydraulic turbine regulating system based on HBBC in frequency control mode," Power System Protection and Control, vol. 51, no. 13, pp. 60-69, Jul. 2023. (in Chinese)

[6] D. Liu, X. Wang, and Y. Peng et al., "Stability analysis of hydropower units under full operating conditions considering turbine nonlinearity," Renewable Energy, vol. 154, pp. 723-742, 2020.

[7] Y. Zheng, Q. J. Chen, and D. L. Yan et al., "Equivalent circuit modelling of large hydropower plants with complex tailrace system for ultra-low frequency oscillation analysis," Applied Mathematical Modelling, vol. 103, pp. 176-194, Mar. 2022.

[8] J. I. Sarasua, G. Martinez-Lucas, and M. Lafoz, "Analysis of alternative frequency control schemes for increasing renewable energy penetration in El Hierro Island power system," International Journal of Electrical Power & Energy Systems, vol. 113, pp. 807-823, Dec. 2019.

[9] W. Fu, K. Wang, and J. Tan et al., "Vibration tendency prediction approach for hydropower generator fused with multiscale dominant ingredient chaotic analysis, adaptive mutation grey wolf optimizer, and KELM," Complexity, vol. 2020, Feb. 2020.

[10] G. Magdy, G. Shabib, and A. A. Elbaset et al., "Decentralized optimal LFC for a real hybrid power system considering renewable energy sources," Journal of En-

gineering Science and Technology, vol. 14, pp. 682-697, Apr. 2019.

[11] C. Lv, Y. H. Xu, and X. Wu *et al.*, "Characteristic analysis and optimal regulation of primary frequency regulation condition in low water head area based on hydraulic-mechanical-electrical coupling model of pumped storage unit," *Complexity*, vol. 2020, Jan. 2020.

[12] T. Piraisoodi, W. I. M. Siluvairaj, and M. A. K. Kappuva, "Multi-objective robust fuzzy fractional order proportional-integral-derivative controller design for nonlinear hydraulic turbine governing system using evolutionary computation techniques," *Expert Systems*, vol. 36, Apr. 2019.

[13] X. Wu, Y. H. Xu, and J. Liu *et al.*, "Characteristics analysis and fuzzy fractional-order PID parameter optimization for primary frequency modulation of a pumped storage unit based on a multi-objective gravitational search algorithm," *Energies*, vol. 13, Jan. 2020.

[14] Y. H. Xu, Y. Zheng, and Y. Du *et al.*, "Adaptive condition predictive-fuzzy PID optimal control of start-up process for pumped storage unit at low head area," *Energy Conversion and Management*, vol. 177, pp. 592-604, Dec. 2018.

[15] R. D. Zhang, Z. X. Cao, and C. M. Bo *et al.*, "New PID controller design using extended nonminimal state space model based predictive functional control structure," *Industrial & Engineering Chemistry Research*, vol. 53, pp. 3283-3292, Feb. 2014.

[16] Z. H. Xiao, S. L. Meng, and N. Lu *et al.*, "One-step-ahead predictive control for hydroturbine governor," *Mathematical Problems in Engineering*, vol. 2015, Jan. 2015.

[17] J. Z. Zhou, Z. G. Zhao, and C. Zhang *et al.*, "a real-time accurate model and its predictive fuzzy PID controller for pumped storage unit via error compensation," *Energies*, vol. 11, Jan. 2018.

[18] A. Kumar, M. N. Anwar, and S. Kumar, "Sliding mode controller design for frequency regulation in an interconnected power system," *Protection and Control of Modern Power Systems*, vol. 6, no. 1, pp. 77-88, Jan. 2021.

[19] Y. Zhou and X. H. Chang, "Event-triggered quantized L-2 - L-infinity filtering for neural networks under denial-of-service attacks," *International Journal of Robust and Nonlinear Control*, vol. 32, pp. 5897-5918, Jul. 2022.

[20] D. Chen, M. L. Zhang, and C. B. Zhang *et al.*, "Research on hydraulic-electric interference and optimisation of multi-turbine hydropower system based on the dual control mode," *IET Renewable Power Generation*, vol. 13, pp. 1096-1104, May 2019.

[21] J. Chen, Z. Xiao, and D. Liu *et al.*, "Nonlinear modeling of hydroturbine dynamic characteristics using LSTM neural network with feedback," *Energy Science & Engineering*, vol. 9, pp. 1961-1972, Nov. 2021.

[22] D. Liu, C. S. Li, and O. P. Malik, "Nonlinear modeling and multi-scale damping characteristics of hydro-turbine regulation systems under complex variable hydraulic and electrical network structures," *Applied Energy*, vol. 293, Jul. 2021.

[23] L. Wang, Y. Zeng, and T. Chen, "Back propagation neural network with adaptive differential evolution al-

gorithm for time series forecasting," *Expert Systems with Applications*, vol. 42, pp. 855-863, Feb. 2015.

[24] J. Chen, Y. Zheng, and X. Deng *et al.*, "Design of a progressive fault diagnosis system for hydropower units considering unknown faults," *Measurement Science and Technology*, vol. 35, p. 015904, 2023.

[25] Y. Liu and W. Guo, "Multi-frequency dynamic performance of hydropower plant under coupling effect of power grid and turbine regulating system with surge tank," *Renewable Energy*, vol. 171, pp. 557-581, Jun. 2021.

[26] H. Li, D. Chen, and H. Zhang *et al.*, "Hamiltonian analysis of a hydro-energy generation system in the transient of sudden load increasing," *Applied Energy*, vol. 185, pp. 244-253, Jan. 2017.

[27] C. Li, J. Zhou, and J. Xiao *et al.*, "Hydraulic turbine governing system identification using T S fuzzy model optimized by chaotic gravitational search algorithm," *Engineering Applications of Artificial Intelligence*, vol. 26, pp. 2073-2082, Oct. 2013.

[28] W. C. Guo, J. D. Yang, and W. J. Yang *et al.*, "Regulation quality for frequency response of turbine regulating system of isolated hydroelectric power plant with surge tank," *International Journal of Electrical Power & Energy Systems*, vol. 73, pp. 528-538, Dec. 2015.

[29] M. Brezovec, I. Kuzle, and M. Krpan *et al.*, "Improved dynamic model of a bulb turbine-generator for analysing oscillations caused by mechanical torque disturbance on a runner blade," *International Journal of Electrical Power & Energy Systems*, vol. 119, Jul. 2020.

[30] W. Guo, J. Yang, and M. Wang *et al.*, "Nonlinear modeling and stability analysis of hydro-turbine governing system with sloping ceiling tailrace tunnel under load disturbance," *Energy Conversion and Management*, vol. 106, pp. 127-138, Dec. 2015.

[31] J. Liang, X. Yuan, and Y. Yuan *et al.*, "Nonlinear dynamic analysis and robust controller design for Francis hydraulic turbine regulating system with a straight-tube surge tank," *Mechanical Systems and Signal Processing*, vol. 85, pp. 927-946, Feb. 2017.

[32] W. Yang, J. Yang, and W. Zeng *et al.*, "Experimental investigation of theoretical stability regions for ultra-low frequency oscillations of hydropower generating systems," *Energy*, vol. 186, Nov. 2019.

[33] X. Yu, X. Yang, and J. Zhang, "Stability analysis of hydro-turbine governing system including surge tanks under interconnected operation during small load disturbance," *Renewable Energy*, vol. 133, pp. 1426-1435, Apr. 2019.

[34] A. Habibollahzade, P. Ahmadi, and M. A. Rosen, "Biomass gasification using various gasification agents: Optimum feedstock selection, detailed numerical analyses and tri-objective grey wolf optimization," *Journal of Cleaner Production*, vol. 284, Feb. 2021.

[35] Z. K. Zhang, Q. H. Tang, and L. P. Zhang, "Mathematical model and grey wolf optimization for low-carbon and low-noise U-shaped robotic assembly line balancing problem," *Journal of Cleaner Production*, vol. 215, pp. 744-756, Apr. 2019.

[36] S. Luo, L. X. Zhang, and Y. S. Fan, "Energy-efficient scheduling for multi-objective flexible job shops with variable processing speeds by grey wolf optimization,"

Journal of Cleaner Production, vol. 234, pp. 1365-1384, Oct. 2019.

[37] U. Sultana, A. B. Khairuddin, and A. S. Mokhtar *et al*., "Grey wolf optimizer based placement and sizing of multiple distributed generation in the distribution system," *Energy*, vol. 111, pp. 525-536, Sep. 2016.

[38] M. Pradhan, P. K. Roy, and T. Pal, "Grey wolf optimization applied to economic load dispatch problems," *International Journal of Electrical Power & Energy Systems*, vol. 83, pp. 325-334, Dec. 2016.

[39] K. P. S. Rana, V. Kumar, and N. Sehgal *et al*., "A Novel dP/dI feedback based control scheme using GWO tuned PID controller for efficient MPPT of PEM fuel cell," *Isa Transactions*, vol. 93, pp. 312-324, Oct. 2019.

[40] M. Niu, Y. Wang, and S. Sun *et al*., "A novel hybrid decomposition-and-ensemble model based on CEEMD and GWO for short-term PM2.5 concentration forecasting," *Atmospheric Environment*, vol. 134, pp. 168-180, Jun. 2016.

[41] A. Meng, C. Zeng, and P. Wang *et al*., "A high-performance crisscross search based grey wolf optimizer for solving optimal power flow problem," *Energy*, vol. 225, Jun. 2021.

[42] M. Yu, D. Lan, and C. Jiang *et al*., "Hybrid condition monitoring of nonlinear mechatronic system using biogeography-based optimization particle filter and optimized extreme learning machine," *ISA Transactions*, vol. 120, pp. 342-359, Jan. 2022.

[43] Z. Gao, J. Zhao, and Y. Hu *et al*., "The challenge for the nature-inspired global optimization algorithms: non-symmetric benchmark functions," *IEEE Access*, vol. 9, pp. 106317-106339, 2021.

[44] M. A. Sanchez, O. Castillo, and J. R. Castro, "Generalized type-2 fuzzy systems for controlling a mobile robot and a performance comparison with interval type-2 and type-1 fuzzy systems," *Expert Systems with Applications*, vol. 42, pp. 5904-5914, Aug. 2015.

[45] E. Ontiveros-Robles, P. Melin, and O. Castillo, "Comparative analysis of noise robustness of type 2 fuzzy logic controllers," *Kybernetika*, vol. 54, pp. 175-201, 2018.

[46] G. J. Geng and Z. G. Guan, "Application of capital asset pricing model based on BP neural network in E-commerce financing," *Computational Intelligence and Neuroscience*, vol. 2022, Aug. 2022.

[47] D. L. J. Alexander, A. Tropsha, and D. A. Winkler, "Beware of R-2: simple, unambiguous assessment of the prediction accuracy of QSAR and QSPR models," *Journal of Chemical Information and Modeling*, vol. 55, pp. 1316-1322, Jul. 2015.

[48] Y. Guo, D. F. Yang, and Y. Zhang *et al*., "Online estimation of SOH for lithium-ion battery based on SSA-Elman neural network," *Protection and Control of Modern Power Systems*, vol. 7, no. 3, pp. 602-618, Dec. 2022.

[49] D. Gerbet and K. Robenack, "Application of LaSalle's invariance principle on polynomial differential equations using quantifier elimination," *IEEE Transactions on Automatic Control*, vol. 67, pp. 3590-3597, Jul. 2022.

[50] D. Derigs, A. R. Winters, and G. J. Gassner *et al*., "A novel averaging technique for discrete entropy-stable dissipation operators for ideal MHD," *Journal of Computational Physics*, vol. 330, pp. 624-632, 2017.